Changes in the Hyperelastic Properties of Endothelial Cells Induced by Tumor Necrosis Factor-α

Inkyung Kang, Dinesh Panneerselvam, Vassilis P. Panoskaltsis, Steven J. Eppell, Roger E. Marchant, and Claire M. Doerschuk

Division of Integrative Biology, Department of Pediatrics, Rainbow Babies and Children's Hospital and Case Western Reserve University and the Department of Biomedical Engineering and Department of Civil Engineering, Case Western Reserve University, Cleveland, Ohio

ABSTRACT Mechanical properties of living cells can be determined using atomic force microscopy (AFM). In this study, a novel analysis was developed to determine the mechanical properties of adherent monolayers of pulmonary microvascular endothelial cells (ECs) using AFM and finite element modeling, which considers both the finite thickness of ECs and their nonlinear elastic properties, as well as the large strain induced by AFM. Comparison of this model with the more traditional Hertzian model, which assumes linear elastic behavior, small strains, and infinite cell thickness, suggests that the new analysis can predict the mechanical response of ECs during AFM indentation better than Hertz's model, especially when using force-displacement data obtained from large indentations (>100 nm). The shear moduli and distensibility of ECs were greater when using small indentations (<100 nm) compared to large indentations (>100 nm). Tumor necrosis factor-α induced changes in the mechanical properties of ECs, which included a decrease in the average shear moduli that occurred in all regions of the ECs and an increase in distensibility in the central regions when measured using small indentations. These changes can be modeled as changes in a chain network structure within the ECs.

INTRODUCTION

Changes in the mechanical properties of tissues and living cells accompany numerous pathophysiological processes, including inflammation, certain forms of cancer, and cardiovascular disease (1–4). Elucidating the mechanisms of these changes associated with pathophysiological processes requires determining the mechanical properties at the cellular and subcellular level using models that can approximate the mechanical response of the cells. Mechanical properties of living cells are usually determined by analyzing the stress-strain or force-displacement relationship. Atomic force microscopy (AFM) is one technique used to measure the force-displacement relationship of the cells by recording the displacement of cells in response to the force applied by the AFM probe (5). AFM has the capability of measuring force-displacement curves combined with topographical information, providing spatial maps of mechanical properties over the apical surface of the living cells.

Traditional analyses of AFM indentation of adherent cells are based on analytical solutions of force-displacement relationships during contact between a rigid indenter and an elastic half-space, assuming that the strain is infinitesimal (6,7). However, these analyses have two major problems. First, the half-space assumption (i.e., the cell is infinitely thick) is not biologically relevant for indentation on the thin adherent cells, and second, the infinitesimal strain is not theoretically relevant for the large strain applied by AFM probe. Previously, analytical solutions for the contact problem of the indentation made by a rigid indenter on an elastic layer of finite thickness were derived using linear elastic theory based on the assumptions that strain levels are small (8–11). These solutions were applied in recent studies for analyzing a spherical AFM probe pressing on an elastic layer of finite thickness (12,13). In these studies, microspheres were attached to the AFM tip to distribute the load applied by the AFM cantilever, which allowed the use of small strain elastic theory. While an elegant approach, these relatively large beads did not allow for the full lateral resolution possible, with a bare AFM tip, to be used. Performing these experiments using a standard AFM cantilever with a sharp pyramidal tip to compress thin regions of adherent cells with a thickness of <1 μm requires a theoretical model that considers the resulting large strains.

Previous studies used finite element modeling to simulate AFM indentation and determined the cellular strains induced by the indenter, or examined the effect of indentation depth, tip geometry, and material nonlinearity on the finite indentation response (14,15). Na et al. (16) generated a theoretical framework for incorporating the nonlinear kinematics and material responses as well as the finite thickness of the cells by developing constitutive models of the thin adherent cells and using finite element modeling to simulate qualitative mechanical responses during AFM nanoindentation. Other investigators used finite element modeling to simulate the AFM nanoindentation on fibroblasts and fungal hyphae to predict the quantitative changes in the mechanical properties of fibroblasts during cytoskeleton disassembly and to determine the elastic response of the cell wall (17,18). Ohashi et al. (19) determined the nonlinear elastic properties of endothelial cells before and after exposure to shear stress using finite

Submitted October 11, 2006, and accepted for publication September 17, 2007.

Address reprint requests to Claire M. Doerschuk, Tel.: 919-966-1077; E-mail: cmd22@med.unc.edu.

Editor: Elliot L. Elson.

0006-3495/08/04/3273/13 $2.00

doi: 10.1529/biophysj.106.099333

element modeling, in which they modified the traditional Hertz's equation describing the force-displacement relationship by adding a first-order term of displacement. Finite element modeling of axisymmetric microindentation tests has been used to determine nonlinear elastic parameters of limb, brain, heel pad, liver, and breast tissues (3,20–24).

Our study built upon these studies by developing a mechanical model of contact between the rigid AFM indenter and thin adherent cells that incorporated both nonlinear kinematics and nonlinear material properties of the cells. Using this model, the mechanical properties of living cells were determined from the AFM force-displacement data using the eight-chain hyperelastic model developed by Arruda and Boyce (25) and employing finite element analysis. The eight-chain model predicted the mechanical response of endothelial cells better than the traditional analysis using Hertz's model, especially when using large indentations (>100 nm). This approach was used to determine the mechanical properties of confluent monolayers of endothelial cells, as well as the effect of tumor necrosis factor-α (TNF-α) on the mechanical properties. TNF-α is a proinflammatory cytokine secreted by macrophages, endothelial cells, and other cells during an inflammatory response. TNF-α induces intracellular signaling pathways in endothelial cells, resulting in increased surface expression of adhesion molecules, remodeling of cytoskeletal components including F-actin and microtubule, and disruption of endothelial barrier function (26–31). Our results demonstrate that TNF-α induces a global decrease in shear moduli, which can be modeled as changes in a chain network structure within the endothelial cells (ECs).

METHODS

Linear elastic constitutive model and the eight-chain model

The models most widely used in AFM studies of mechanical properties of biological materials are based on Hertz's and Sneddon's studies (6,7). Hertz's theory is used to model the contact between two elastic spheres based on Hooke's law assuming linear elastic constitutive relationships. The constitutive equation according to Hooke's law may be derived from the following free energy function,

$$\Psi = \mu tr(\boldsymbol{\epsilon}^2) + \frac{1}{2}\gamma(tr\boldsymbol{\epsilon})^2, \tag{1}$$

in which Ψ = Helmholtz free energy function, μ and γ are the two constants of Lamé, and $\boldsymbol{\varepsilon}$ is the small strain tensor.

In this study, the constitutive relationship for the cell was selected to be the eight-chain model, which is a hyperelastic model originally developed by Arruda and Boyce (25) to describe the mechanical responses of incompressible rubber composed of a polymer chain network structure. The constitutive models using limiting chain distensibility are applicable to modeling the mechanical response of soft biological tissues such as arterial walls (32). The eight-chain model was used in our analysis, since this theory predicts the strain-hardening behavior of an incompressible material using two material constants—shear moduli and distensibility. Moreover, the structural properties of the polymer chain network can be calculated from the mechanical properties provided by the eight-chain model. The eight-chain model was previously used to determine mechanical properties of human skin tissue, considering the mechanical effects of filamentous collagen networks within the tissue (33).

The constitutive relationship of the eight-chain model for an isotropic and incompressible material is derived from the following free energy function (25),

$$\Psi = \mu_{8\text{chain}}\left[\frac{1}{2}(I_1 - 3) + \frac{1}{20\lambda_L^2}(I_1^2 - 9) + \frac{11}{1050\lambda_L^4}(I_1^3 - 27) + \frac{19}{7000\lambda_L^6}(I_1^4 - 81) + \frac{519}{673,750\lambda_L^8}(I_1^5 - 243)\right] + \ldots, \tag{2}$$

where $\mu_{8\text{chain}}$ = shear moduli; I_1 = first invariant of the right Cauchy-Green strain tensor $\mathbf{C}$, which is related to the Green-Lagrangian strain tensor $\mathbf{E}$ as $\mathbf{C} = 2\mathbf{E} + \mathbf{I}$ where I is the rank 2 unit tensor; and λ_L = distensibility or limiting network stretch, the ratio of the contour length to the initial end-to-end length of a polymeric chain, r_L/r_0. The five-term approximation of the eight-chain model is used in this study. In this study, the endothelial cell was assumed to be incompressible as previously reported (34,35).

Comparison of Hertz's model and the eight-chain hyperelastic model for the uniaxial extension

The Hertz's model describes the relationship between force and displacement during a contact between two bodies and is based on Hooke's law. This model is appropriate for materials subjected to small deformations of <1%. However, the eight-chain model was originally developed for incompressible polymeric materials subjected to large deformations, and is based on the assumption that the elasticity of the material is dependent only on the entropic changes in the chain network configuration.

Computational stress-stretch relationships during a uniaxial stretch of a linear elastic incompressible material (ν = Poisson's ratio = 0.5) can be determined using Hooke's law as

$$\sigma_{\text{Hooke}} = E\varepsilon = 2(1+\nu)\mu_{\text{Hooke}}(\lambda - 1) = 3\mu_{\text{Hooke}}(\lambda - 1), \tag{3}$$

where Young's modulus is E and the stretch λ is defined as the ratio of deformed length to the initial length.

When using the eight-chain model, the stress-stretch relationships during a uniaxial stretch are given as

$$\sigma_{8\text{chain}} = 2\left(\lambda^2 - \frac{1}{\lambda}\right)\frac{\partial\Psi}{\partial I_1}. \tag{4}$$

Using the definition in Eq. 2,

$$\sigma_{8\text{chain}} = 2\mu_{8\text{chain}}\left(\lambda^2 - \frac{1}{\lambda}\right)\left(\frac{1}{2} + \frac{2I_1}{20N} + \frac{33I_1^2}{1050N^2} + \frac{76I_1^3}{7000N^3} + \frac{519I_1^4}{673750N^4}\right), \tag{5}$$

where $I_1 = \lambda^2 + 2/\lambda$ for the uniaxial stretch, and $N = \lambda_L^2$.

The computational stress-stretch curves for the Hooke's law and the eight-chain model were determined from Eqs. 3 and 5, assuming a constant shear moduli ($\mu_{8\text{chain}}$ and μ_{Hooke}) of 1 Pa and the distensibility (λ_L) of the eight-chain model varying between 2 and 4 as shown in Fig. 1 *A*. When the distensibility λ_L decreased, the stress-stretch curves from the eight-chain model showed a greater degree of strain-hardening and deviated further away from linear stretch-stretch curve defined by Hooke's law (Fig. 1 *A*).

The elastic moduli can be calculated as the slope of the stress-stretch curve when the stretch is one, which is $3\mu_{\text{Hooke}}$ for Hooke's law, and

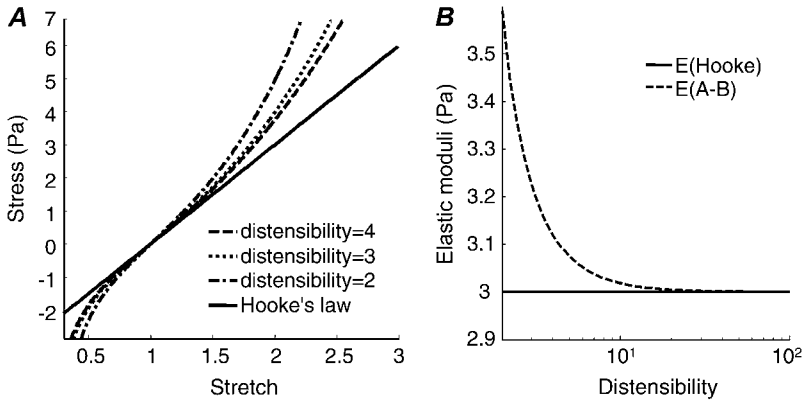

FIGURE 1 The computational stress-stretch curve (*A*) and the elastic moduli determined as the initial slope of the stress-stretch curve (*B*) during uniaxial stretch determined using the eight-chain model and Hooke's law when μ_{8chain} and μ_{Hooke} are = 1 Pa. (*A*) Stress-stretch curves exhibited greater strain-hardening behavior upon decreasing λ_L (distensibility) in contrast to the linear relationship predicted by Hooke's law. (*B*) The elastic moduli from Arruda-Boyce model and from Hooke's model (*E*(8*chain*) and *E*(*Hooke*)) are calculated as the initial slope of the stress-stretch curve in panel *A* when stretch = 1. When the distensibility is large, *E*(8*chain*) is similar to *E*(*Hooke*), but increases rapidly as the distensibility decreases toward unity.

$(\partial\sigma_{8chain}/\partial\lambda)|_{\lambda=1}$ for the eight-chain model. When distensibility is large, the elastic modulus of the eight-chain model is similar to the Hooke's model, which is three times the shear modulus (μ_{Hooke}). As the distensibility approaches unity, the elastic modulus increases rapidly in the Arruda-Boyce model (Fig. 1 *B*). These observations underline the very different physical bases of these two models.

Modeling AFM indentations on cells

Hertz's model for blunt-conical indenters

Hertz's original solution was based on the contact between two elastic spheres, and Sneddon modified Hertz's solution to different geometries of the indenter, including cylindrical and conical indenters. A modified Hertzian model for the indenters with blunt-conical geometry was also reported, which is close to the geometry of a typical AFM probe (36). This modified model gives the following force-displacement relationship for a blunt-conical probe with a spherical tip with radius r, half-open angle θ, contact radius a, and point of transition between cone and sphere $b = r\cos\theta$, pressing with a displacement w_0 on a linear elastic semi-infinite half-space with Young's modulus E and Poisson's ratio ν, when

$$w_0 \le \frac{b^2}{r}, \quad F = \frac{4E}{3(1-\nu^2)} r^{1/2} w_0^{3/2}, \tag{6}$$

and when

$$w_0 \ge \frac{b^2}{r},\ F = \frac{2E}{(1-\nu^2)}\left\{ a w_0 - \frac{a^2}{2\tan\theta}\left[\frac{\pi}{2} - \arcsin\left(\frac{b}{a}\right)\right] - \frac{a^3}{3r} + (a^2-b^2)^{1/2}\left(\frac{b}{2\tan\theta} + \frac{a^2-b^2}{3r}\right)\right\}, \tag{7}$$

with the contact radius a calculated from the equation

$$w_0 + \frac{a}{r}\left((a^2-b^2)^{1/2} - a\right) - \frac{a}{\tan\theta}\left[\frac{\pi}{2} - \arcsin\left(\frac{b}{a}\right)\right] = 0. \tag{8}$$

Hyperelastic finite element analysis using the eight-chain constitutive model

Finite element analysis is widely used to simulate the mechanical behaviors of materials and structures without using an analytical solution. This is useful because analytical solutions are often not available for the mechanical problems in the case of complicated geometry, large deformation, or nonlinear material constitutive relationships. AFM indentation on thin adherent cells was modeled as an axisymmetric compression by a rigid blunt-conical probe with tip radius of 100 nm and half-open angle of 37.5° on a hyperelastic layer using a finite element program Abaqus 6.4.1 (Abaqus, Providence, RI, Fig. 2 *A*). A nominal Young's modulus of silicon nitride used for the standard AFM probe is ~300 GPa, which is at least six orders-of-magnitude greater than the highest value of elastic moduli (~100 kPa) of ECs measured by AFM. Based on this, the indenter was assumed rigid in the finite element modeling. During our indentation experiments, the maximum value of compressive force was typically in the range of 1–2 nN, which was modeled by applying a concentrated force of 1.5 nN on the rigid blunt-conical indenter in the direction parallel to the axis of symmetry, resulting in compression of a layer under the indenter. The cell was modeled as an incompressible, isotropic, and homogeneous disk with a density of 1 g/cm^3 and a radius of 30 μm. The thickness of the cell was varied between 0.5 and 3 μm. The cell consisted of minimum of 5939 to maximum of 18,968 nodes distributed over 2727–9241 deformable axisymmetric six-node triangular hybrid shell elements. Near the contact region between the cell and the rigid indenter, a biased mesh was used to generate greater numbers of elements.

Boundary conditions used in the finite element analysis

The axisymmetric axis is given as axis 2 as depicted in Fig. 2 *A*. Boundary conditions during the compression were given as follows:

1. No displacement along the axis 1 or 2 at the bottom face of the hyperelastic layer, to model the firm adhesion of the cell on the substrate (U1 = U2 = 0).
2. No displacement along the axis 1 along the axisymmetric axis of the cell (U1 = 0).
3. No displacement along the axis 1, and no rotation around the axis 3 for the rigid indenter (U1 = UR3 = 0).

The AFM indentation was simulated by applying a concentrated force of 1.5 nN on the reference point of the rigid indenter in the −2 direction, resulting in deformation of the cell. The contact between the rigid probe and the cell was modeled as a frictionless, finite-sliding interaction between a deformable and a rigid body, which is used to allow separation and sliding of finite amplitude and arbitrary rotation of the surfaces.

Experimental procedure

Measuring force-displacement data on adherent endothelial cells using AFM

Human pulmonary microvascular endothelial cells (ECs) were purchased from Cambrex (Walkersville, MD) and plated on fibronectin-coated glass

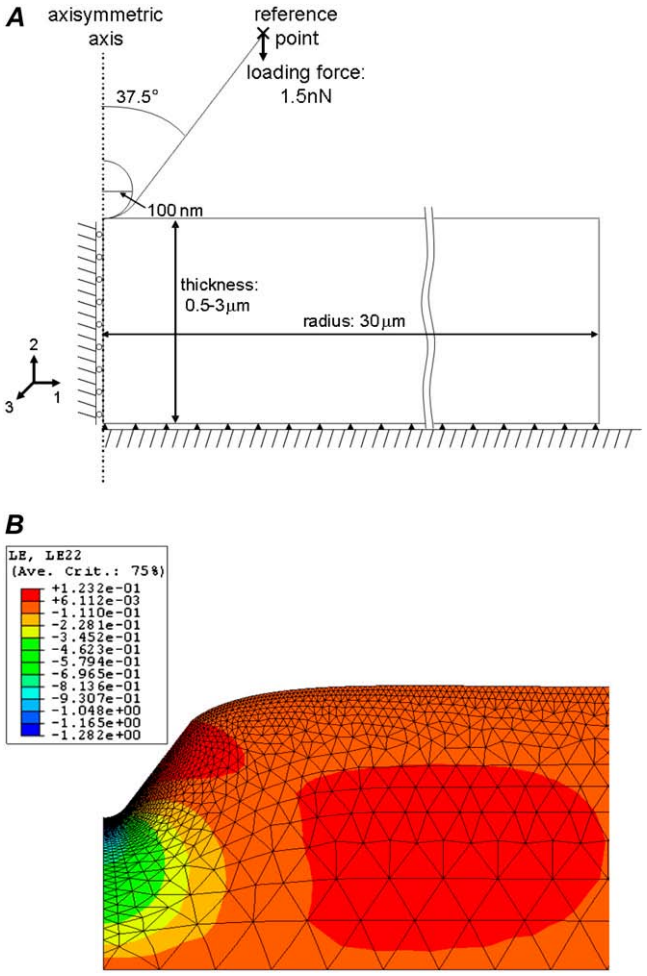

FIGURE 2 Finite element models of AFM indentation on thin adherent cells. (*A*) The contact between the AFM probe and a confluent layer of thin adherent cells was modeled as an axisymmetric compression by a rigid blunt-conical indenter with tip radius of 100 nm and half-open angle of 37.5° on a thin layer by using Abaqus 6.4.1. The three axes of the configuration are depicted as 1, 2, and 3 along with the direction of the axes. (*B*) Strain field in the thin adherent layer of cells during AFM indentation computed by FEM. Strain in perpendicular direction (LE22) reached up to ~130% in the elements under the center of the probe, indicating that the regions near this element suffered large strain during AFM indentation.

coverslips according to manufacturer's protocols. Confluent ECs between passages 7 and 15 were exposed to buffer only (10 μl of 0.1% bovine serum albumin in PBS added to 1 ml of culture media) or to TNF-α (equal volume in the same buffer added to 1ml of culture media, final concentration of 20 ng/ml) for 4 or 24 h before experiments. AFM images and force-displacement curves of ECs were obtained using a Nanoscope IV Bioscope AFM (Digital Instruments, Santa Barbara, CA) equipped with a G-type scanner, and a silicon nitride cantilever/probe with nominal spring constant of 0.06 N/m (Digital Instruments). AFM data of the ECs were obtained while the cells were covered with culture medium. Force-maps were generated by obtaining a cycle of loading and unloading force-displacement curves at every pixel on a topographical image. All AFM data were obtained at room temperature (25°C), and each force-displacement curve was obtained with a rate of 8 Hz. All images were obtained in a square area of 10,000 μm^2 consisting of 64 × 64 data points (pixel size 1.56 μm). The range of Z-displacement during force-displacement data acquisition was 1 μm, and the loading rate of each force curve was 0.125 μm/s.

Visualization of F-actin distribution in endothelial cells

Confluent ECs between passages 7 and 15 were used. ECs were exposed to TNF-α (20 ng/ml, R&D Systems, Minneapolis, MN) for 0, 4, or 24 h before experiments. These cells were fixed with 0.1% paraformaldehyde and incubated with fluorescein isothiocyanate-labeled phalloidin (0.66×10^{-6} M, Sigma, St. Louis, MO) for 0.5 h. The coverslips were mounted using a mounting media containing DAPI for fluorescent labeling of DNA (Vector Laboratories, Burlingame, CA). The cells were imaged using a Leica TCS SP2 AOBS laser scanning confocal microscope (Leica Microsystems, Heidelberg, Germany). For each area, a stack of images with 0.2 μm of section width was taken, and an average projection image was generated using Leica Confocal Software 2.0 (Leica Microsystems).

Analysis of the mechanical properties of the ECs

Determining thickness of each spatial position of ECs from the AFM force map

The thickness of each pixel of the ECs was calculated by combining topographical information and deformations calculated from the force-displacement data. Since the topographical information is relative, a reference value for the underlying substrate was necessary to calculate the thickness of the cell; the minimum value in the topographical image was used for this reference value since it represents the baseline height of the substrate exposed between the ECs. The deformed height of each pixel was calculated by subtracting this single reference value from the relative height value of each pixel in the topographical image measured by AFM.

The contact point between the AFM probe and the EC was identified in the force-displacement curve as the point where the difference between the force-displacement curve and a straight line through a point 500 nm away on the x axis from the starting point (x_0–500 nm, y_0) and the last point (x_{max}, y_{max}) of the curve was maximal. Topographical information recorded by AFM is the height of the pixel after a given compressive force is applied by the probe, and thus, represents the thickness of the cell after deformation. The deformation of each pixel of the force map was calculated as the indentation depth in the force-displacement data. Therefore, the actual thickness for each pixel is calculated from the relative height of the pixel minus the minimum height in the topographical image plus the indentation depth from force-displacement data of the pixel.

Simulating mechanical responses of thin adherent cells during AFM indentation using finite element modeling

AFM indentation on a confluent monolayer of the ECs grown on cell culture polystyrene dish was modeled as a rigid blunt-conical indenter pressing on a hyperelastic layer adherent on a rigid substrate using finite element analysis as described in Modeling AFM Indentations on Cells. Logarithmic strain **LE** is defined as

$$\mathbf{LE} = \ln \mathbf{v} = \sum_{i=1}^{3} \ln \lambda_i \mathbf{n}_i \mathbf{n}_i^T, \quad (9)$$

where $\mathbf{v} = \sqrt{\mathbf{F}\mathbf{F}^T}$ is the left stretch tensor, λ_i the principal stretches, and $\mathbf{n}_i$ the principal stretch directions in this configuration (i.e., Eigen vectors of $\mathbf{v}$). Logarithmic strain in the direction parallel to the axis 2 (LE22) was computed after a compressive force of 1.5 nN was applied by the rigid blunt-conical indenter on a 1-μm thick cell with μ_{8chain} of 500 Pa and λ_L of 1.05 (Fig. 2 *B*). LE22 reached up to ~130% in the elements under the center of the probe, indicating that the cell suffers a large strain during AFM indentation. The indentation depth reached up to ~450 nm which is close to the experimental results of 300 ~500 nm.

The effects of varying μ_{8chain}, thickness, and λ_L of the eight-chain model on the computational force-displacement data generated using finite element modeling of AFM indentation, were determined (Fig. 3, *A–C*). When the

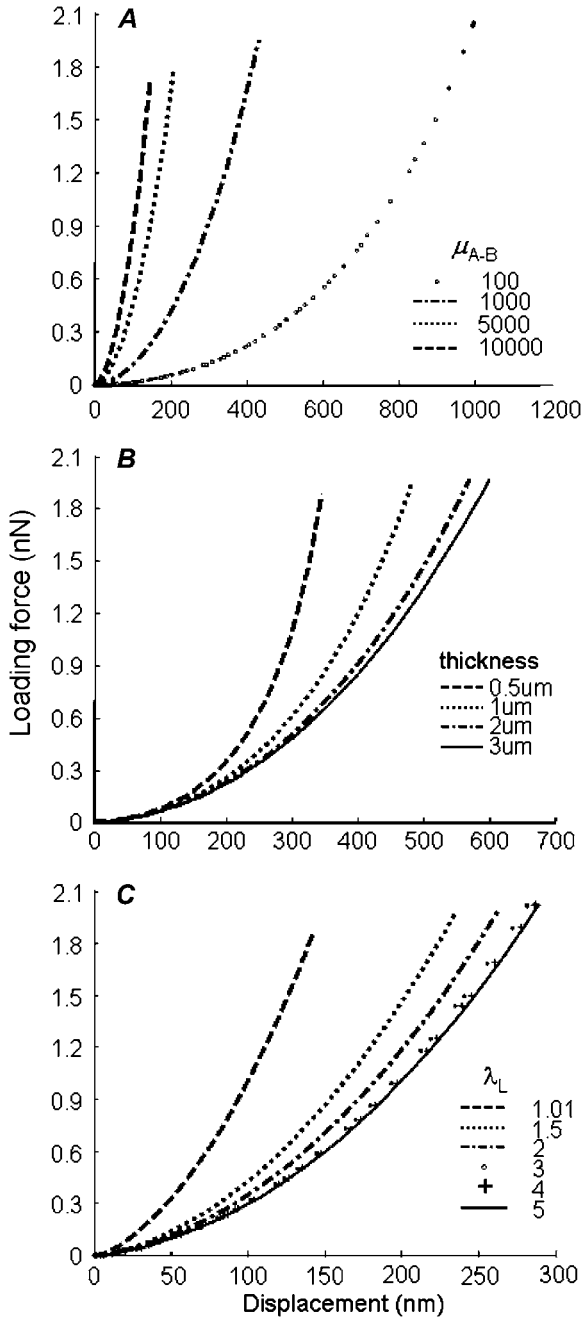

FIGURE 3 FEM force-displacement data during AFM indentation. (*A*) Force-displacement curves upon varying shear moduli from 100 to 10,000 Pa with fixed values of λ_L at 1.05 and thickness at 2 μm. (*B*) Force-displacement curves upon varying the thickness from 0.5 to 3 μm with fixed values of λ_L at 1.05 and μ_{8chain} at 500 Pa. The force increased at the same value of displacement when the thickness decreased, especially in the range of <1 μm. (*C*) Force-displacement upon varying λ_L from 1.01 to 5 with fixed μ_{8chain} at 5000 Pa and thickness at 2 μm. Decreased distensibility of the polymer chain network (λ_L) within the material resulted in increased force at the same displacement.

shear moduli were varied from 100 to 10,000 Pa while the distensibility and thickness were held constant at 1.05 and 2 μm, the force-displacement data exhibited the greatest changes in the range of shear moduli values between 100 and 1000 Pa, as shown in Fig. 3 *A*. When the thickness was decreased from 3 μm to 0.5 μm while the other parameters were fixed at λ_L of 1.05 and μ_{8chain} of 500 Pa, the force was greater at the same value of displacement (Fig. 3 *B*). As the sample thickness decreased, the same displacement results in a larger strain and therefore a larger stress, thus increasing the load needed to attain that displacement. The distensibility was varied in the range of 1.01 to 3, which is the reported range of the parameter for biological tissues (24,33). Lower values of λ_L resulted in higher forces corresponding to the same displacement as shown in Fig. 3 *C*, indicating that the material appears stiffer when distensibility of polymer network within the material is decreased, as expected by the definition of distensibility.

Based on these results, variable intervals were used for μ_{8chain}, 500 Pa in the range of 100 and 1000 Pa, 1000 Pa between 1000 and 5000 Pa, 5000 Pa between 5000 and 50,000 Pa, and 10,000 Pa between 50,000 and 100,000 Pa (Table 1). Similarly, the distensibility or limiting network stretch of 1.01, 1.05, 1.1, 1.2, 1.3, 1.5, 2.0, 2.5, and 3 were chosen to generate computational force-displacement curves using the eight-chain hyperelastic finite element models (FEMs) (Table 1). The computation of force-displacement data took between 20 and 120 min for each combination of parameters using a personal computer with a Pentium IV 2.4 GHz processor and 512 MB RAM.

Determining the mechanical properties of the cell by comparing experimental and computational force-displacement curves

To determine the mechanical properties of the living cells, the AFM force-displacement data were compared to the computational force-displacement relationship from the eight-chain hyperelastic FEMs (Fig. 4). Since computation of force-displacement data took between 20 and 120 min for each variation of parameters and the number of force-displacement data per AFM force map exceeded 4000, performing curve fitting for each experimental force-displacement curve could not be completed within a reasonable amount of time. To expedite the analysis, the following approach was used in our study.

First, FEMs of indentations were generated by varying thickness, distensibility, and μ_{8chain} parameters of the cell using a custom-written code in Python 2.0 (Python Software Foundation, Ipswich, MA). For each combination of these parameters, AFM indentation on the cell was simulated using Abaqus 6.4.1, and the magnitude of force and displacement in axis 2 (U2) were recorded. As a result, a database of computational force-displacement curves was generated for all the possible combination of the three parameters varying within the given range (Table 1).

Second, the thickness obtained from the experimental data was compared to the computational database from the FEMs, and the subset of the computational data with the closest thickness was selected. The unloading part of the experimental force-displacement data was compared with the computed force-displacement data within the selected FEMs, and the difference between the experimental data and the model was calculated using the coefficient of correlation (R^2), which represents the fit between the model and experimental data. The coefficient of correlation is defined as

$$R^2 = 1 - \frac{SS_E}{SS_T} = 1 - \frac{\sum_{i=1}^{n}(y_i - \hat{y}_i)^2}{\sum_{i=1}^{n}(y_i - \bar{y})^2}, \qquad (10)$$

TABLE 1 Range of material parameters used in the analysis

Parameter	Range
Thickness	0.5–3 μm with increments of 0.5 μm
μ_{8chain}	100, 500, 1000, 2000, 3000, 4000, 5000, 10,000, 15,000, 20,000, 25,000, 30,000, 35,000, 40,000, 45,000, 50,000, 60,000, 70,000, 80,000, 90,000, 100,000
λ_L	1.01, 1.05, 1.1, 1.2, 1.3, 1.5, 2, 2.5, 3

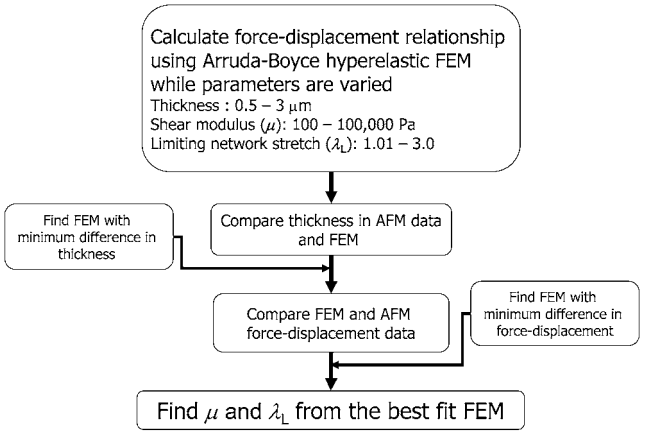

FIGURE 4 Flow diagram of the parametric approach for determining the mechanical properties using finite element analysis. A database of computational force-displacement curves was generated using parameters varying between 0.5 and 3 μm for the thickness, 1.01–3 for the distensibility, and 100–100,000 Pa for the shear moduli in the eight-chain hyperelastic FEMs. For each combination of the thickness and shear modulus parameters, AFM indentation on the cell was simulated while recording the magnitude of total force (TF:magnitude) and displacement in axis 2 (U2) at the reference point of the rigid indenter. The thickness of the EC region at which the AFM data was determined and compared with the thickness used in all FEMs. A subset of FEMs with the closest thickness was selected. AFM force-displacement data were then compared with the force-displacement data from the subset of FEMs, and the mechanical properties were determined from the shear modulus and distensibility of the best fit FEMs.

where SS_E is error sum of squares, SS_T is total corrected sum of squares, y_i is the i^{th} point of the experimental data, $\hat{y}_i$ is the i^{th} point of the computational data from the FEMs, $\bar{y}$ is the mean of the experimental data, and n is the number of the points in the experimental data. The distensibility and the shear modulus were determined from the parameters in the computational data from the FEMs that had the greatest R^2 value for the force-displacement data. The pixels with R^2 values ≤ 0 were excluded from the analysis.

The experimental and computational force-displacement data are defined in different discrete domains. To compare the two data, the computational data were represented by a polynomial equation determined from a standard least-squares curve-fitting module, Polyfit, in MatLab 7.0.1 (The MathWorks, Natick, MA), in which the R^2 values exceeded 0.999 in all curve fittings. The experimental force-displacement data were compared to the polynomial representation of the computational data. The R^2 values between the experimental and the polynomial representation of computational data were calculated using a custom-written code in MatLab 7.0.1.

Determining hyperelastic properties in different regions of ECs

To determine the mechanical responses of ECs during small and large indentations, the total range of indentation depths in the AFM and computational force-displacement curves were divided into two regions: the indentation depths of 0–100 nm, and >100 nm. The indentation depth of 100 nm exceeds the thickness of the phospholipid bilayer of a cell membrane, which is ~5 nm. Because of our choice of digitization rate in collecting the data, AFM force-displacement data within 5 nm of indentation depth did not include enough data points to determine elastic moduli. Moduli were obtainable within 100 nm of displacement, and this depth may include the molecules expressed on the cell surface, such as glycocalyx, plasma membrane, membrane-bound F-actin, and the linker proteins that bind F-actin to the plasma membrane. Mechanical properties were determined from the best fit FEM of the AFM data as depicted in Fig. 5. The shear moduli from the eight-chain model were categorized according to the indentation depths used in determining them, $\mu_{8chain\ 0\text{-}100nm}$ for indentation depths 0–100 nm, $\mu_{8chain>100nm}$ for indentation depths >100 nm, and $\mu_{8chain\ total}$ for the total indentation depths.

Average shear moduli and distensibility were determined for the entire surface of each cell, except for the tall area near nuclei. The regions overlying nuclei were outlined by hand in the topographical images and excluded in the analysis, since the height of these regions often exceeded the vertical scanning range of our AFM. Subsequently, each cell was divided into peripheral (within 10 μm from cell borders) and central regions. Maps of peripheral and central regions of each cell were outlined from the topographical AFM images using ImageJ (National Institutes of Health, Bethesda, MD). The average mechanical properties for the peripheral, central, and entire region of each cell were determined from the maps of elastic moduli derived from each region using a custom-made program in MatLab 7.0.1.

Determining elastic properties using Hertz's model

The shear moduli of the ECs from the finite element analysis were compared to the shear moduli determined from the same cells using the blunt-conical Hertz's model described in Eqs. 6–8.

Shear moduli were calculated from Young's moduli (E) determined in the Hertz's model and Poisson's ratio (ν) as in Eq. 11,

$$\mu_{Hertz} = \frac{E}{2(1+\nu)}. \tag{11}$$

In the analysis using the blunt-conical Hertz's model described in Eqs. 6–8, the cells were assumed to be incompressible, i.e., Poisson's ratio was assumed to be 0.5.

The Hertzian shear moduli for different ranges of indentation depths, $\mu_{Hertz\ total}$, $\mu_{Hertz\ 0\text{-}100nm}$, and $\mu_{Hertz>100nm}$, were determined by optimization of the elastic moduli parameter in Hertz's force-displacement equations for each range using the Nelder-Mead simplex algorithm (37). The average $\mu_{Hertz\ total}$, $\mu_{Hertz\ 0\text{-}100nm}$, and $\mu_{Hertz>100nm}$ values from Hertz's model were determined in the different regions of the ECs as described above.

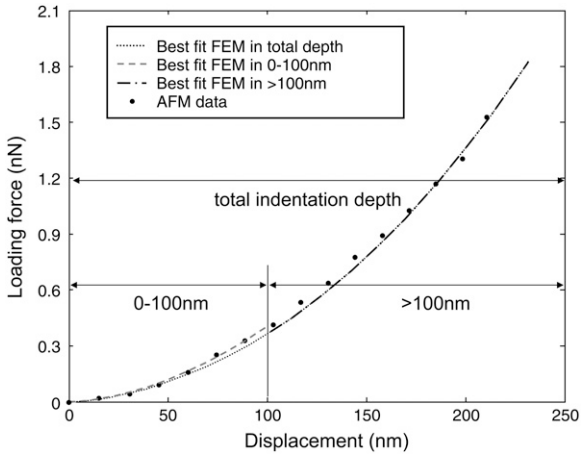

FIGURE 5 Determining mechanical properties from AFM force-displacement data measured on ECs using FEM. The thickness of EC at which AFM data was obtained was determined from the height in the AFM topography image and the indentation depth in the force-displacement data. The force-displacement data were divided according to the indentation depth of 0–100 nm, >100 nm, and in the total indentation depth. The mechanical properties in these indentation depths were determined from the best-fit FEMs that simulate the experimental force-displacement curve most closely.

Statistical analysis

Mechanical properties are expressed as average ± standard error unless otherwise specified. Differences in the shear moduli were identified by paired student's *t*-tests for the comparison of the shear moduli of different regions of the same cell and by one-way ANOVA for the comparison of more than two groups. Differences were regarded significant if $P < 0.05$.

RESULTS

Mechanical properties of the ECs were determined using the eight-chain hyperelastic FEMs and Hertz's model

The mechanical properties of the confluent monolayers of ECs without TNF-α treatment were determined from the experimental force-displacement curve generated from each pixel of the AFM force maps, and reconstructed as maps of thickness, $R^2_{8\text{chain}}$, $\mu_{8\text{chain}}$, and λ_L. Representative maps of thickness, $R^2_{8\text{chain}}$, $\mu_{8\text{chain total}}$, and λ_L values are shown in Fig. 6, *A–D*. In Fig. 6 *A*, topographical information is given as the value of each pixel, which is represented as the color scale shown in the bar on the right. Taller regions such as regions containing nuclei appear brighter in Fig. 6 *A*. Fig. 6 *B* is a map of the coefficients of correlation, $R^2_{8\text{chain}}$ (Eq. 10). The value of each pixel is a measure of how closely the computational hyperelastic force-displacement curve from the FEMs fits the experimental force-displacement data of that pixel, the brighter pixels meaning greater $R^2_{8\text{chain}}$ values. Regions containing nuclei of the ECs were often taller than the upper limit of thickness used in the FEM (*open pixels*, Fig. 6 *A*), and are solid areas in the map of $R^2_{8\text{chain}}$ (*solid arrows* in Fig. 6 *B*). Except for the regions containing nuclei, most of the area covered by cells exhibited R^2 value >0.9, indicating that the ranges of parameters used in creating the database of computational force-displacement curves from the FEMs were sufficient to predict mechanical behavior of the cells with good agreement.

Fig. 6, *C* and *D*, shows maps of hyperelastic material constants, $\mu_{8\text{chain total}}$ and λ_L, used in the FEMs that generated the best-fit computational force-displacement curve to the experimental data for each pixel. The map of λ_L (Fig. 6 *D*) showed that the distensibility of ECs had a high variability in the range of values used in the analysis, between 1.01 and 3.

The average values for $\mu_{8\text{chain total}}$, $\mu_{8\text{chain 0-100nm}}$, and $\mu_{8\text{chain}>100\text{nm}}$ were determined for each EC ($N = 15$ cells from five AFM images). The average values of $\mu_{\text{Hertz total}}$, $\mu_{\text{Hertz 0-100nm}}$, and $\mu_{\text{Hertz}>100\text{nm}}$ of the same cells were determined using Hertz's model. Images of $\mu_{\text{Hertz total}}$ and

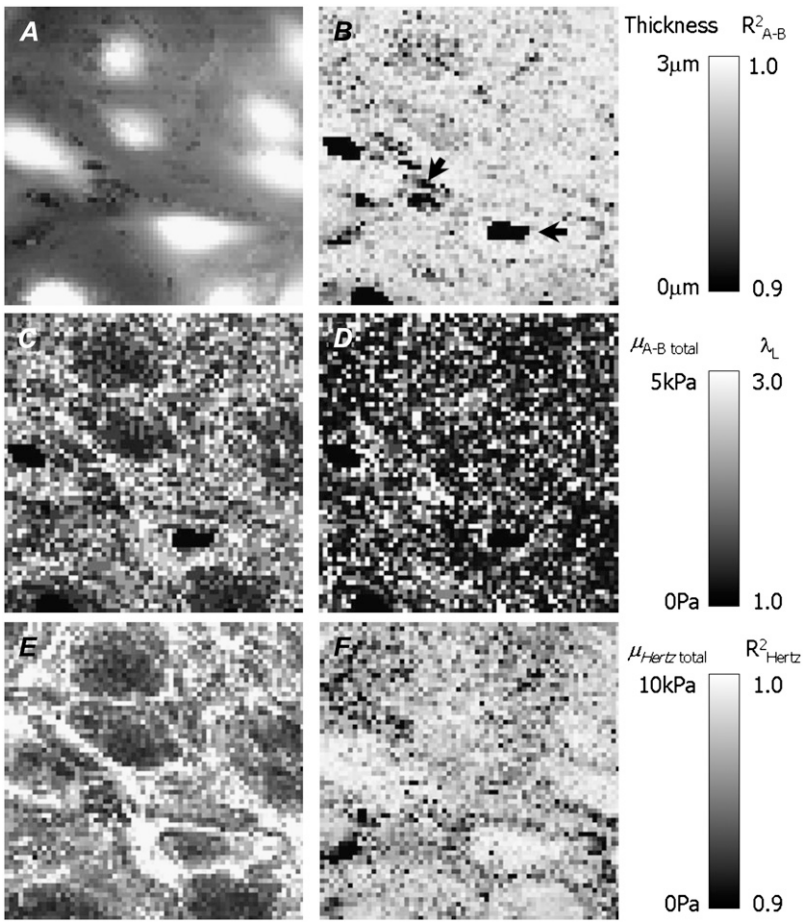

FIGURE 6 Maps of thickness (*A*), $R^2_{8\text{chain}}$ (*B*), $\mu_{8\text{chain total}}$ (*C*), λ_L (*D*), $E_{\text{Hertz total}}$ (*E*), and R^2_{Hertz} (*F*) of a representative region of EC monolayers. Scale bars in the right represent the range of the values of thickness, $R^2_{8\text{chain}}$, $\mu_{8\text{chain}}$, λ_L, $E_{\text{Hertz total}}$, and R^2_{Hertz} in each map. Regions near nuclei with thickness >3 μm or near cell junctions with thickness <0.5 μm correspond to dark areas in $R^2_{8\text{chain}}$ map (*solid arrows* in *B*), because the thickness of these regions falls out of the range used in the FEMs.

R^2_{Hertz} are shown in Fig. 6, *E* and *F*, for the same cells as in Fig. 6, *A–D*.

The average $\mu_{8chain\ total}$ value of the entire surface of ECs determined using finite element modeling was 2815 ± 163 Pa. The average $\mu_{8chain\ total}$ values of the central and peripheral regions were 2667 ± 191 Pa and 2929 ± 160 Pa, respectively. The average $\mu_{Hertz\ total}$ values were 6791 ± 490 Pa, 6349 ± 555 Pa, and 7159 ± 467 Pa, for the entire surface and the central and peripheral regions, respectively.

For each region, $\mu_{8chain\ total}$ was $\ll \mu_{Hertz\ total}$. The average μ_{Hertz} value for the entire surface is ~2.4 times greater than the average μ_{8chain} value for total indentation depths, 2.5 times for indentations >100 nm, and 1.7 times for indentations of 0–100 nm. Fig. 1, *A* and *B*, indicates that the eight-chain model predicts that the stress-stretch curve will have a greater initial slope than the Hooke's model for the same shear modulus and that the stress-stretch curve from the eight-chain model appears stiffer than Hooke's curve as stretch increases, which is due to strain-hardening. Thus, if the same experimental force-displacement data were analyzed using the eight-chain model, the shear modulus would appear less than when using Hertz's model, and the differences between the two moduli would become greater for large indentations compared to small indentations.

To determine the fit of the eight-chain model and Hertz's model to the mechanical response of ECs during AFM indentation, the R^2 values for Hertz's model and for the eight-chain model were compared (Fig. 7, *A* and *B*). A representative example presented in Fig. 7 *A* shows that the eight-chain model closely matched experimental force-displacement data to a higher degree than Hertz's model, as shown by the greater R^2 value. The average R^2_{Hertz} was $>R^2_{8chain}$ in 0–100 nm indentations (Fig. 7 *B*), likely due to multiple iterations of parameters during the simplex search optimization method from the analysis using Hertz's model, but not when the eight-chain model was used. Notably, R^2_{8chain} was $>R^2_{Hertz}$ in >100 nm indentations despite the coarse-step optimization process used for the hyperelastic FEMs; this suggests that the mechanical properties of ECs in large indentation depths are better modeled using a hyperelastic constitutive model such as the eight-chain, rather than the linear-elastic, model.

Average shear moduli and distensibility of ECs were greater when using indentations 0–100 nm than indentations >100 nm

Mechanical properties of ECs were determined using the eight-chain and Hertz's models averaged over entire surface of each EC and in the peripheral and central regions for 0–100 nm and >100 nm indentations. The values of $\mu_{8chain\ 0\text{-}100nm}$ were significantly greater than $\mu_{8chain>100nm}$ when averaged over the entire surface and in the peripheral and central regions of the ECs (Fig. 8 *A*, $P < 0.001$). Distensibility (λ_L) of ECs was greater for indentations of 0–100 nm than for indentations >100 nm (Fig. 8 *B*, $P < 0.001$). In contrast, when analyzed using Hertz's model, the values of $\mu_{Hertz\ 0\text{-}100nm}$ were not significantly different from $\mu_{Hertz\ >100nm}$ in any of the cell regions (Fig. 8 *C*).

TNF-α induced F-actin cytoskeletal remodeling and a decrease in shear moduli of ECs

Remodeling of F-actin in ECs induced by TNF-α was demonstrated by F-actin staining (Fig. 9, *A–C*). Before TNF-α treatment, most of the F-actin was found in peripheral bands near the intercellular junctions (Fig. 9 *A*). TNF-α induced disruption of the well-defined peripheral bands and an increase in F-actin stress fibers in the cell body after 4 h of treatment (Fig. 9 *B*). After 24 h of TNF-α treatment, ECs became elongated in shape, and F-actin stress fibers were increased in numbers and rearranged in parallel to the long axis of the cell body (Fig. 9 *C*).

The average $\mu_{8chain\ total}$, $\mu_{8chain\ 0\text{-}100nm}$, and $\mu_{8chain>100nm}$ or $\mu_{Hertz\ total}$, $\mu_{Hertz\ 0\text{-}100nm}$, and $\mu_{Hertz>100nm}$ values of ECs treated with TNF-α for 0, 4, and 24 h were determined for the entire EC surface, and in the central and peripheral regions of the ECs (Fig. 10, *A–D*). TNF-α induced a significant decrease in the average $\mu_{8chain\ total}$ for the peripheral and central regions of ECs after 24 h of treatment (data not shown, $P < 0.01$). TNF-α induced a significant decrease in the average $\mu_{8chain\ 0\text{-}100nm}$ in the central and peripheral regions of the ECs after 4 and 24 h of treatment ($P < 0.01$, Fig. 10 *A*). The average $\mu_{8chain\ >100nm}$ exhibited similar changes in the

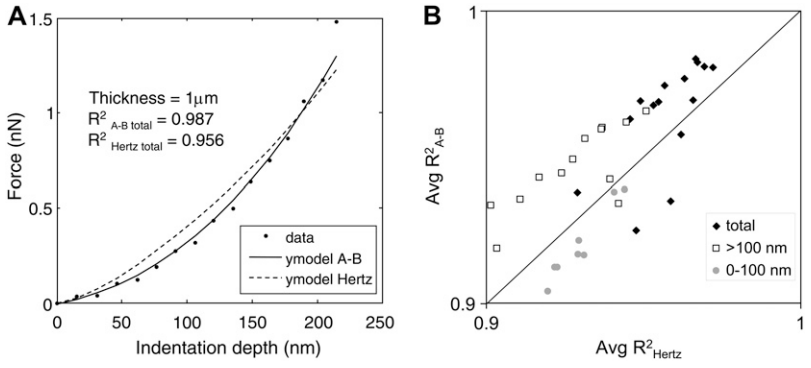

FIGURE 7 The fit of the eight-chain model and Hertz's model to the AFM force-displacement data. (*A*) A representative example shows that the eight-chain model mimicked experimental force-displacement data closer than Hertz's model, as indicated by the greater R^2 value. (*B*) R^2_{8chain} and R^2_{Hertz} averaged for entire area of each EC when using the eight-chain model or Hertz's model for the entire indentation depths, and for 0–100 nm and >100 nm indentations are shown.

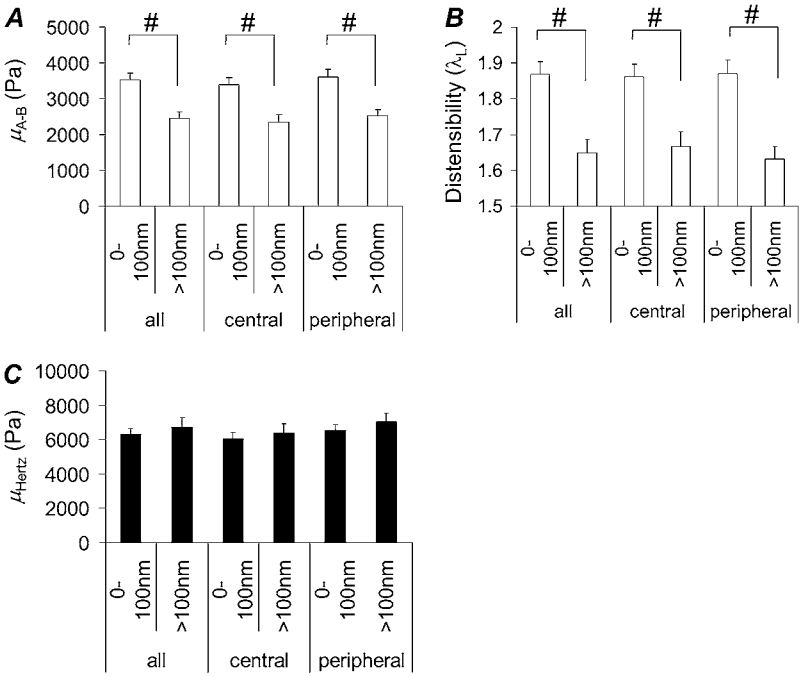

FIGURE 8 The average shear moduli (*A*) and distensibility (*B*) for 0–100 nm and >100 nm of indentation depths for the entire surface, peripheral, and central regions from the FEMs and the average $\mu_{8chain\ 0\text{-}100nm}$ and $\mu_{8chain>100nm}$ from Hertz's model (*C*). The values $\mu_{8chain\ 0\text{-}100nm}$ were $\gg\mu_{8chain>100nm}$ in the entire surface, peripheral, and central regions of the ECs when analyzed using FEM (#-columns in panel *A*, $P < 0.05$). The value λ_L was significantly greater in the indentation depths 0–100 nm than in the depths >100 nm (#-columns in panel *B*, $P < 0.05$). When Hertz's model was used in the analysis, $\mu_{Hertz\ 0\text{–}100nm}$ were not significantly different from $\mu_{Hertz\ >\ 100nm}$ in any region of the cells.

central and peripheral regions after 24 h of TNF-α treatment ($P < 0.05$, Fig. 10 *B*). When analyzed using Hertz's model, a significant decrease in $\mu_{Hertz\ 0\text{-}100nm}$ was found for the entire EC surface and in the central regions after 24 h of TNF-α treatment ($P < 0.05$, Fig. 10 *C*). The value of $\mu_{Hertz>100nm}$ tended to decrease, but not significantly (Fig. 10 *D*).

TNF-α induced a significant increase in the average distensibility (λ_L) in the central regions for 0–100 nm depths after 4 h of treatment (Fig. 11 *A*), but not when analyzed using indentation depths >100 nm (Fig. 11 *B*).

DISCUSSION

In this study, a novel analysis was developed to determine subcellular mechanical properties of adherent ECs using AFM and finite element modeling. This analysis used mechanical models that incorporated the finite thickness and nonlinear elasticity of the cells as well as the large strain induced by AFM, which are more physiologically relevant and theoretically accurate than the traditional analysis using Hertz's model. Using this analysis, our data demonstrate that the mechanical responses of the ECs measured using small (<100 nm) or large (>100 nm) indentation depths are different. The ECs appeared stiffer when the mechanical properties were calculated using small compared to large indentation depths. The data also show that TNF-α induced changes in the mechanical properties of ECs. The average shear moduli (μ_{8chain}) decreased in the central and peripheral regions. The distensibility of the TNF-α-treated ECs increased in the central regions when measured using a small indentation.

The force-displacement curves obtained during AFM indentation have inherent nonlinearity for several reasons that make analyses complex. Hertz's model does consider the constantly changing contact area between the AFM tip and the cell surface, one source of nonlinearity. However, other sources of nonlinearities are likely important to consider in analyzing the force-displacement curves during AFM indentation. For example, during loading on cells adherent to a rigid substrate, strain levels within the cells often exceed the

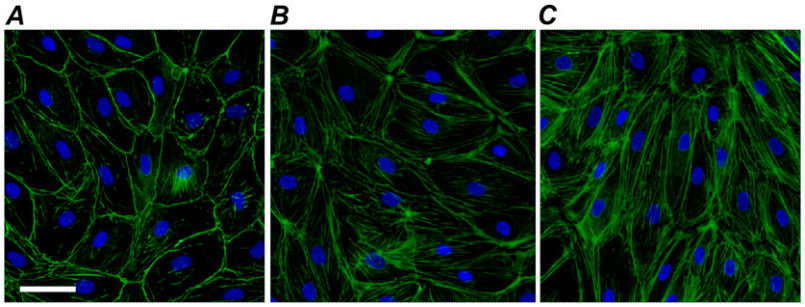

FIGURE 9 Representative confocal laser scanning microscopy images of the ECs stained against F-actin (*green*) and nuclei (*blue*) after 0 (*A*), 4 (*B*), and 24 (*C*) h of TNF-α treatment. (*A*) Most F-actin was in peripheral bands near intercellular junctions before TNF-α treatment. (*B*) After 4 h of TNF-α treatment, the peripheral bands were disrupted, and more F-actin stress fibers were observed in the central region of the ECs. (*C*) After 24 h of TNF-α treatment, ECs were elongated in shape and F-actin stress fibers were increased. Scale bar = 50 μm.

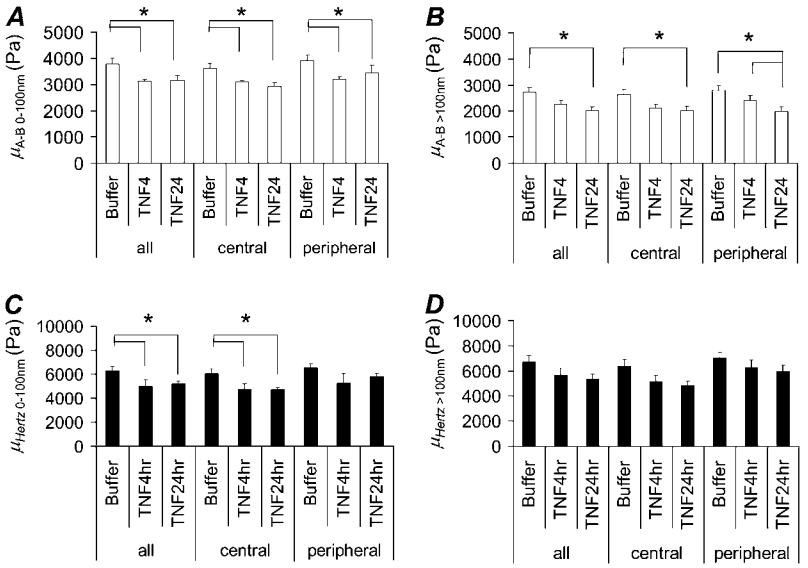

FIGURE 10 The average values of $\mu_{8chain\ 0\text{-}100nm}$, $\mu_{8chain>100nm}$, $\mu_{Hertz\ 0\text{-}100nm}$, and $\mu_{Hertz>100nm}$ (*A–D*) for the entire surface, for the central and peripheral regions of ECs before and after TNF-α treatment for 4 and 24 h. (*A*) The average $\mu_{8chain\ 0\text{-}100nm}$ values of ECs were significantly lower than controls after 4 and 24 h of TNF-α treatment in the entire EC surface and in the central and peripheral regions ($P < 0.05$). (*B*) The average $\mu_{8chain>100nm}$ values exhibited similar changes for the entire EC surface and in the central and peripheral regions after 24 h of TNF-α treatment ($P < 0.05$). (*C*) The average $\mu_{Hertz\ 0\text{-}100nm}$ values for the entire EC surface and for the central regions were significantly lower than controls after 4 and 24 h of TNF-α treatment ($P < 0.05$). (*D*) The values of $\mu_{Hertz>100nm}$ tended to decrease, but not significantly.

range suitable for small strain theory, and the mechanical response of the cells is nonlinear. Thus, hyperelastic constitutive models are appropriate in modeling the mechanical response of flat adherent cells. The eight-chain model is one of the hyperelastic constitutive models intended to describe the entropy change upon stretching long-chain molecules. The eight-chain model was used in our analysis, since this model predicts the strain-hardening behavior of an incompressible material with a simple model that uses two material constants—shear moduli and distensibility. These constants are related to the structural properties of the polymeric chain network of rubbery materials, which include chain density and number of rigid segments within a chain. The mechanical properties of human skin tissues were determined using the eight-chain model, in which the filamentous collagen networks within the tissue were taken into account (33).

To process the large amount of data which is required to construct maps of subcellular properties of entire cell surface, a computational force-displacement database was created using parameters of thickness, distensibility, and shear moduli that were varied using the intervals described in Table 1. This database was compared with the experimental force-displacement data. The mechanical properties were determined from the best-fit model within the database of computational force-displacement data which estimated the experimental force curve with minimum error. The nonlinear elastic properties of ECs determined using this approach were able to predict the mechanical response of the cells during AFM indentations with the coefficient of correlations almost as good or better than Hertz's model.

Several assumptions were made in our approach to generating these results. First, the eight-chain model assumes the cells are an isotropic material and that the changes induced by TNF-α may not be isotropic. Thus, our isotropic eight-chain model might only approximate the anisotropic changes induced by TNF-α. Second, the model assumes that the cells are homogeneous. Our approach to this problem was to measure the force-displacement curve on each pixel of 1.6×1.6 μm in size, and to divide each curve into 0–100 nm and >100 nm in the indentation depths, so that the mechanical properties of different regions of ECs can be more accurately determined. Third, the finite element modeling assumes that the indentation was performed away from the outer boundaries of the cells. To account for this, pixels with thickness

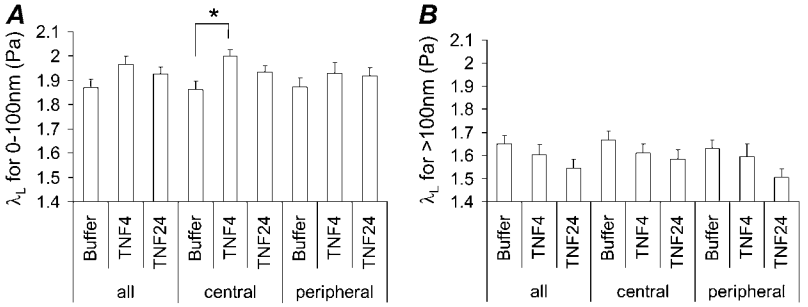

FIGURE 11 The average λ_L values for (*A*) 0–100 nm and (*B*) >100 nm of indentation depths for the entire surface and for the central and peripheral regions of ECs before and after TNF-α treatment for 4 and 24 h. (*A*) The average λ_L value for 0–100 nm in the central region was significantly greater than controls after 4 h of TNF-α treatment ($P < 0.05$). (*B*) The λ_L-value for >100 nm tended to be lower than controls after 24 h of TNF-α treatment, but not significantly.

<0.25 μm were excluded from the analysis. The ECs were confluent monolayers at the time of the experiment, and thus, only a few cells had a free outer edge. Fourth, the hyperelastic properties of ECs were obtained by the eight-chain finite element model that maximizes the fit with the experimental data within the range of 100–100,000 Pa in shear modulus and 1.01–3 in distensibility. Thus, the hyperelastic properties determined in this study represent a unique solution within these physiologically relevant ranges.

When the eight-chain model was used to determine the mechanical properties of ECs, the average $R^2_{8\text{chain}}$ was $<R^2_{\text{Hertz}}$ in 0–100 nm indentations, whereas the opposite was true when indentations were >100 nm (Fig. 7 *B*). The optimization method used in the analysis based on the eight-chain model did not allow multiple iterations of parameters and was thus unlike the simplex search optimization method used in the analysis based on Hertz's model. Therefore, it is not surprising that $R^2_{8\text{chain}}$ was $<R^2_{\text{Hertz}}$ when the indentations were small. However, our finding that $R^2_{8\text{chain}}$ was $>R^2_{\text{Hertz}}$ in >100 nm indentations strongly suggests that the mechanical properties of ECs in large indentation depths are modeled more accurately when using a hyperelastic constitutive model such as the eight-chain model, which accounts for strain-hardening behavior, compared to a linear-elastic model such as Hertz's.

The average shear moduli and the distensibility of ECs determined from the finite element modeling were greater when calculated using small indentations (<100 nm) than large indentations (>100 nm). At least four possibilities may account for this difference:

1. Different regions of the cells are probed with small compared to large indentations, and the micromechanical properties of ECs may vary in these different regions. For example, the superficial regions (<100 nm) may be stiffer than the underlying regions (>100 nm), or the mechanical properties probed in the small area of cell-probe contact during small indentations of 0–100 nm may differ from those probed in the larger contact area during indentations >100 nm.
2. The shear moduli in the large indentations or the distensibility in the small indentations might have not accurately determined, since the mechanical behavior during the small indentations is dictated by the shear moduli more heavily than the distensibility, and the opposite is true in the large indentations.
3. The superficial regions of ECs may exhibit smaller shear moduli and distensibility when displaced by large indentations after the small indentations than when displaced by only small indentations. This may be due to the strain-softening of the superficial regions themselves when indented >100 nm by the AFM probe.
4. The computed value of strain-hardening (as quantified by the curvature of the force-displacement curve) might exceed the actual degree of strain-hardening of ECs during AFM indentation. The degree of strain-hardening is dictated by the range of distensibility used in the model.

This study used a range between 1.01 and 3.0, based on our observations that distensibility values >3.0 did not alter the computational force-displacement curves generated from the eight-chain hyperelastic FEMs with shear modulus of 200 Pa and thickness of 2 μm (Fig. 3 *C*). However, this may not be the case when thicknesses or shear moduli are very small or large. A model that overestimates strain-hardening would result in lower values of moduli and distensibility than the actual values and thus a decrease in these parameters as strain increased. Another caveat of our findings is that although our data found the differences in the mechanical properties for indentations <100 nm compared to >100 nm, the mechanical properties are not likely to be discretely different at 100-nm indentation, but instead change continuously during progressively deeper indentations.

When ECs were treated with TNF-α, the average shear moduli were significantly lower than controls not treated with TNF-α. The average $\mu_{8\text{chain 0-100nm}}$ and $\mu_{8\text{chain}>100\text{nm}}$ significantly decreased in the central and peripheral regions. Even though Hertz's model provides a poorer fit, the values show similar results in that $\mu_{\text{Hertz 0-100nm}}$ decreased when averaged over the entire surface and in the central regions, and $\mu_{\text{Hertz}>100\text{nm}}$ tended to decrease but not significantly. Our results are consistent with our previous observation that the stiffness of ECs decreased significantly after 4 h of TNF-α treatment when measured using magnetic bead twisting cytometry (Q. Wang and C. M. Doerschuk, unpublished observation). Remodeling of the F-actin network inside the cells may be responsible for this decrease in EC stiffness, despite in vitro data suggesting that F-actin stress fibers are stiffer than F-actin microfilaments or G-actin. Intriguingly, the eight-chain model predicts that the decrease in the shear moduli is due to a decrease in the density of chains, which may happen during the formation of thick bundles of stress fibers from thinner F-actin filaments during TNF-α treatment. Furthermore, the changes in ECs induced by TNF-α such as the expression of adhesion molecules on the apical membrane, the remodeling of lipid distribution of the membrane, and the remodeling of cytoskeletal components other than F-actin stress fibers might result in a decrease in the stiffness probed by AFM indentation. Finally, disruption of the endothelial junction, induced by TNF-α, affects barrier function of ECs and may relieve the tension generated at the cell-cell junctions or at the cell-extracellular matrix, which in turn may induce a decrease of EC stiffness. Changes in the average distensibility were different when small or large indentations were used in the analysis. When only 0–100 nm of indentations within force-displacement curves were analyzed using the finite element modeling, TNF-α resulted in an increased distensibility in the central region. The distensibility provides a measure of strain-hardening behavior as described in Fig. 1 *A*. Thus, our results that TNF-α induced an increase in EC distensibility in the 0–100 nm of

indentations can be interpreted to suggest that TNF-α induces a decrease in strain-hardening in the central regions near apical membrane as well as a decrease in the stiffness.

In conclusion, a novel analysis was developed to determine the nonlinear elastic properties of endothelial cells using finite element modeling of AFM indentation on flat adherent cells. This analysis predicted the mechanical response of ECs during AFM indentations better than the traditional analysis using Hertz's model especially for large indentations ($>$100 nm). The shear moduli of ECs were greater when measured using force-displacement data obtained from small indentation ($<$100 nm) compared to large indentation ($>$100 nm) depths. Tumor necrosis factor (TNF)-α induced a global decrease in the shear moduli and an increase in the distensibility only in the central region of the ECs when measured using small indentations, which can be modeled as changes in a chain network structure within the ECs.

We thank Dr. Ellen M. Arruda for helpful discussions, Chesong Lee for his assistance on Python programming, and Dr. Qin Wang for her assistance with experiments and discussions.

Supported by grants No. HL048160 and No. HL077370.

REFERENCES

1. Tajaddini, A., D. L. Kilpatrick, and D. G. Vince. 2003. A novel experimental method to estimate stress-strain behavior of intact coronary arteries using intravascular ultrasound (IVUS). *J. Biomech. Eng.* 125:120–123.
2. Kilpatrick, D., C. Xu, R. Vito, and S. Glagov. 2002. Correlation of mechanical behavior and MMP-1 presence in human atherosclerotic plaque. *J. Mech. Med. Biol.* 2:1–7.
3. Samani, A., and D. Plewes. 2004. A method to measure the hyperelastic parameters of ex vivo breast tissue samples. *Phys. Med. Biol.* 49:4395–4405.
4. Krouskop, T. A., T. M. Wheeler, F. Kallel, B. S. Garra, and T. Hall. 1998. Elastic moduli of breast and prostate tissues under compression. *Ultrason. Imaging.* 20:260–274.
5. Marchant, R. E., I. Kang, P. S. Sit, Y. Zhou, B. A. Todd, S. J. Eppell, and I. Lee. 2002. Molecular views and measurements of hemostatic processes using atomic force microscopy. *Curr. Protein Pept. Sci.* 3: 249–274.
6. Hertz, H. 1881. On the contact of elastic solids. *J. Reine Angew. Math.* 92:156–171.
7. Sneddon, I. N. 1965. The relation between load and penetration in the axisymmetric Boussinesq problem for a punch of arbitrary profile. *Int. J. Eng. Sci.* 3:47–57.
8. Lebedev, N. N., and I. S. Ufliand. 1958. Axisymmetric contact problem for an elastic layer. *J. Appl. Math. Mech.* 22:320–326.
9. Chen, W. T., and P. A. Engel. 1972. Impact and contact stress analysis in multilayer media. *Int. J. Solid Struct.* 8:1257–1281.
10. Hayes, W. C., L. M. Keer, G. Herrmann, and L. F. Mockros. 1972. A mathematical analysis for indentation tests of articular cartilage. *J. Biomech.* 5:541–551.
11. Kalaba, R. E., A. Yakush, and E. A. Zagustin. 1976. On a conical punch pressing into an elastic layer. *J. Elast.* 6:441–449.
12. Dimitriadis, E. K., F. Horkay, J. Maresca, B. Kachar, and R. S. Chadwick. 2002. Determination of elastic moduli of thin layers of soft material using the atomic force microscope. *Biophys. J.* 82:2798–2810.
13. Mahaffy, R. E., S. Park, E. Gerde, J. Kas, and C. K. Shih. 2004. Quantitative analysis of the viscoelastic properties of thin regions of fibroblasts using atomic force microscopy. *Biophys. J.* 86:1777–1793.
14. Costa, K. D., and F. C. Yin. 1999. Analysis of indentation: implications for measuring mechanical properties with atomic force microscopy. *J. Biomech. Eng.* 121:462–471.
15. Charras, G. T., and M. A. Horton. 2002. Determination of cellular strains by combined atomic force microscopy and finite element modeling. *Biophys. J.* 83:858–879.
16. Na, S., Z. Sun, G. A. Meininger, and J. D. Humphrey. 2004. On atomic force microscopy and the constitutive behavior of living cells. *Biomech. Model. Mechanobiol.* 3:75–84.
17. Kasas, S., X. Wang, H. Hirling, R. Marsault, B. Huni, A. Yersin, R. Regazzi, G. Grenningloh, B. Riederer, L. Forro, G. Dietler, and S. Catsicas. 2005. Superficial and deep changes of cellular mechanical properties following cytoskeleton disassembly. *Cell Motil. Cytoskeleton.* 62:124–132.
18. Zhao, L., D. Schaefer, H. Xu, S. J. Modi, W. R. LaCourse, and M. R. Marten. 2005. Elastic properties of the cell wall of *Aspergillus nidulans* studied with atomic force microscopy. *Biotechnol. Prog.* 21:292–299.
19. Ohashi, T., Y. Ishii, Y. Ishikawa, T. Matsumoto, and M. Sato. 2002. Experimental and numerical analyses of local mechanical properties measured by atomic force microscopy for sheared endothelial cells. *Biomed. Mater. Eng.* 12:319–327.
20. Tonuk, E., and M. B. Silver-Thorn. 2003. Nonlinear elastic material property estimation of lower extremity residual limb tissues. *IEEE Trans. Neural Syst. Rehabil. Eng.* 11:43–53.
21. Miller, K., and K. Chinzei. 1997. Constitutive modeling of brain tissue: experiment and theory. *J. Biomech.* 30:1115–1121.
22. Miller-Young, J. E., N. A. Duncan, and G. Baroud. 2002. Material properties of the human calcaneal fat pad in compression: experiment and theory. *J. Biomech.* 35:1523–1531.
23. Hu, T., and J. P. Desai. 2004. Characterization of soft-tissue material properties: large deformation analysis. Second International Symposium on Medical Simulation, Proceedings. 28–37.
24. Liu, Y., A. E. Kerdok, and R. D. Howe. 2004. A Nonlinear finite element model of soft tissue indentation. Second International Symposium on Medical Simulation, Proceedings. 67–76.
25. Arruda, E. M., and M. C. Boyce. 1993. A 3-dimensional constitutive model for the large stretch behavior of rubber elastic materials. *J. Mech. Phys. Solids.* 41:389–412.
26. Gamble, J. R., J. M. Harlan, S. J. Klebanoff, and M. A. Vadas. 1985. Stimulation of the adherence of neutrophils to umbilical vein endothelium by human recombinant tumor necrosis factor. *Proc. Natl. Acad. Sci. USA.* 82:8667–8671.
27. Goldblum, S. E., and W. L. Sun. 1990. Tumor necrosis factor-α augments pulmonary arterial transendothelial albumin flux in vitro. *Am. J. Physiol.* 258:L57–L67.
28. Petrache, I., A. D. Verin, M. T. Crow, A. Birukova, F. Liu, and J. G. Garcia. 2001. Differential effect of MLC kinase in TNF-α-induced endothelial cell apoptosis and barrier dysfunction. *Am. J. Physiol. Lung Cell. Mol. Physiol.* 280:L1168–L1178.
29. Deli, M. A., L. Descamps, M. P. Dehouck, R. Cecchelli, F. Joo, C. S. Abraham, and G. Torpier. 1995. Exposure of tumor necrosis factor-α to luminal membrane of bovine brain capillary endothelial cells cocultured with astrocytes induces a delayed increase of permeability and cytoplasmic stress fiber formation of actin. *J. Neurosci. Res.* 41: 717–726.
30. Petrache, I., A. Birukova, S. I. Ramirez, J. G. Garcia, and A. D. Verin. 2003. The role of the microtubules in tumor necrosis factor-α-induced endothelial cell permeability. *Am. J. Respir. Cell Mol. Biol.* 28: 574–581.
31. Molony, L., and L. Armstrong. 1991. Cytoskeletal reorganizations in human umbilical vein endothelial cells as a result of cytokine exposure. *Exp. Cell Res.* 196:40–48.

32. Horgan, C. O., and G. Saccomandi. 2003. A description of arterial wall mechanics using limiting chain extensibility constitutive models. *Biomech. Model. Mechanobiol.* 1:251–266.

33. Bischoff, J. E., E. M. Arruda, and K. Grosh. 2000. Finite element modeling of human skin using an isotropic, nonlinear elastic constitutive model. *J. Biomech.* 33:645–652.

34. Dong, C., J. Cao, E. J. Struble, and H. H. Lipowsky. 1999. Mechanics of leukocyte deformation and adhesion to endothelium in shear flow. *Ann. Biomed. Eng.* 27:298–312.

35. Sato, M., N. Ohshima, and R. M. Nerem. 1996. Viscoelastic properties of cultured porcine aortic endothelial cells exposed to shear stress. *J. Biomech.* 29:461–467.

36. Briscoe, B. J., K. S. Sebastian, and M. J. Adams. 1994. The effect of indenter geometry on the elastic response to indentation. *J. Phys. D Appl. Phys.* 27:1156–1162.

37. Lagarias, J. C., J. A. Reeds, M. H. Wright, and P. E. Wright. 1998. Convergence properties of the Nelder-Mead simplex method in low dimensions. *SIAM J. Optim.* 9:112–147.